Input Refinement with Incremental Learning for Accurate Digital Twin-Enabled Self-Driven QoT Optimization in Optical Networks

XIN YANG[1,2,*], CHENYU SUN[2,3,4], REDA AYASSI[2], LOUIS AKNIN[2,5], GABRIEL CHARLET[2], MASSIMO TORNATORE[1], AND YVAN POINTURIER[2]

[1]*Politecnico di Milano, 20133 Milan, Italy*
[2]*Huawei Technologies France, Paris Research Center, Optical Comm. Tech. Lab, 92100 Boulogne-Billancourt, France*
[3]*EURECOM, Communication Systems Department, 06410 Biot, France*
[4]*Sorbonne Université, 75006 Paris, France*
[5]*Centrale Lyon, 69130 Écully, France*
**Corresponding author: xin.yang@polimi.it*

Received XX Month XXXX; revised XX Month, XXXX; accepted XX Month XXXX; posted XX Month XXXX (Doc. ID XXXXX); published XX Month XXXX

Reliable Quality of Transmission (QoT) prediction is essential to ensure that services operate near their optimal working point, maximizing network capacity and efficiency while avoiding large design margins. A major source of QoT prediction error lies in the uncertain modeling of nonlinear fiber impairments, particularly the Kerr effect and Stimulated Raman Scattering (SRS), which are difficult to monitor with existing hardware. Accurate modeling of these effects requires knowledge of fiber insertion loss. In addition, the gain spectrum of optical amplifiers, which governs Amplified Spontaneous Emission (ASE) noise is not directly monitored. Further uncertainties stem from service end-to-end (E2E) impairments, including Wavelength Selective Switch (WSS) filtering-induced noise and from device-specific back-to-back (B2B) transponder performance, both of which are typically unknown at deployment time. To address these challenges, we propose Incremental Learning-based Input Refinement (IIR), a parameter estimation method that leverages multiple network snapshots to jointly refine fiber insertion losses, amplifier gain spectra, and end-to-end offset noise (comprising WSS filtering and transponder B2B contributions). IIR is applied incrementally during routine, live network (re-)optimization, requiring no intrusive measurements. The proposed method is validated through (1) simulations using experimental data on a C-band ring network, and (2) experimental validation on a C-band mesh network. Results show that IIR significantly improves the estimation of key physical-layer parameters, enhancing QoT prediction accuracy and enabling effective closed-loop power optimization.

1. INTRODUCTION

A. Motivation

Recent advancements in optical network monitoring are opening new opportunities for more effective Quality of Transmission (QoT) (re-) optimization. In optical networks, end-to-end (E2E) services are transmitted over multiple wavelengths and traverse several links or Optical Multiplex Sections (OMSs). The QoT of these services, typically quantified by Bit Error Rate (BER), Q-factor, or Signal-to-Noise Ratio (SNR), is influenced by various physical-layer impairments. Key contributors include fiber nonlinearities such as Kerr effects (including self-phase modulation, cross-phase modulation, and four-wave mixing) and Stimulated Raman Scattering (SRS), both of which are highly sensitive to the launch power into each fiber span. Additionally, Amplified Spontaneous Emission (ASE) noise, generated by Erbium-Doped Fiber Amplifiers (EDFAs) and determined by their gain and noise figure (NF) spectra, directly impacts the Optical SNR (OSNR). Other important impairments include Wavelength Selective Switch (WSS) filtering penalties and the back-to-back (B2B) performance of transponders, both of which can further degrade QoT.

To ensure reliable data transmission, service QoT must consistently remain above a required threshold. Specifically, the BER must stay below, and the SNR above, the Forward Error Correction (FEC) limit. However, service QoT can degrade over time due to 1) load-dependent effects, which vary when services are added or dropped [1,2], and 2) dirty or aged connectors, which affect both nonlinear impairments and ASE noise [3]. Consequently, automated network QoT optimization [1,4,5,6,7,8,9,10] at the physical layer is critical to maintain optimal service performance throughout the network's operational lifespan and prevent service outages.

Digital twin (DT) technology has recently emerged as a powerful tool for QoT prediction [12,13] and optimization [2,11]. A DT allows predictive modeling of network behavior under hypothetical configurations and support what-if scenario analysis. For example, by simulating changes in booster (the first amplifier in an OMS) launch power spectrum, a DT can estimate the potential impact on service quality before the changes are implemented. This capability enables

predictive and non-intrusive QoT optimization.

In this study, we adopt an analytical model-based digital twin, which offers greater transparency, explainability and adaptability than neural network-based approaches [19,20,21,22,23,24,25]. Analytical models explicitly represent key physical-layer effects such as SRS, ASE noise, Kerr nonlinearity, WSS filtering, and transponder B2B performance. The Gaussian Noise (GN) model [26,39], extended to account for SRS, provides a computationally efficient and accurate framework [27]. However, the accuracy of such a DT strongly depends on the accuracy of its input parameters [1,14]. When properly calibrated, the DT enables reliable QoT prediction and effective optimization. If the input parameters are inaccurate, optimization decisions may be suboptimal, resulting in degraded QoT and inefficient resource usage [15].

In practice, several input parameters are difficult to obtain due to limited monitoring capability, such as 1) fiber insertion losses, affecting power entering and propagating along the fiber, hence affecting Kerr and SRS effects; 2) amplifier gain and NF spectra that affects the ASE noise modelling, and 3) E2E offset noise from WSS filtering and transponder B2B performance. Inaccurate estimation of these parameters leads to unreliable QoT prediction and degraded optimization outcomes [28].

To overcome this challenge, network snapshots can serve as a valuable resource. These snapshots, collected by the network management system, represent distinct network states and include physical-layer data such as service information (i.e., routing table, rate), power spectra from Optical Channel Monitors (OCMs), total power readings from photodiodes (PDs) in EDFAs, and BER values observed at the receivers. However, improper use of snapshot data can compromise parameter estimation. For instance, in [29], refining insertion losses and amplifier gain spectra using only a single snapshot led to overfitting of nonlinear impairments. This caused transponder B2B noise and WSS penalties to be misinterpreted, resulting in underestimated insertion loss values.

To address this limitation, we propose a method called Incremental-learning-based Input Refinement (IIR). This technique uses multiple snapshots, collected during a multi-step power optimization process, to incrementally estimate fiber insertion loss, amplifier gain spectrum, and E2E offset noise. By capturing variations across snapshots, the IIR method improves estimation accuracy without overfitting. This allows the construction of a more accurate DT, capable of supporting self-driven QoT optimization in dynamic optical networks.

B. State of the art

Table 1 summarizes several existing techniques for input parameter refinement aimed at improving the accuracy of digital twin (DT) models for optical network optimization. The work in [30] proposed a Bayesian optimization-based algorithm to estimate fiber insertion losses and amplifier noise figures by minimizing the error in Optical Signal-to-Noise Ratio (OSNR) estimation. This method considers only ASE noise and does not account for nonlinear fiber noise, which limits its SNR prediction accuracy. In [31], a method was presented to jointly estimate fiber parameters, including effective area, attenuation coefficient, Raman gain coefficient, and insertion losses, along with the average amplifier noise figure. The approach modifies amplifier gain and tilt settings to minimize the discrepancy between estimated and measured output power spectra and OSNR at the pre-amplifier of each OMS. However, the method assumes homogeneous gain spectra across all EDFAs, which may not reflect real-world conditions. Paper [35] proposes an input refinement paradigm that improves the accuracy of both physics-based and machine learning models for received power estimation after Raman amplifiers in dynamic C+L-band optical networks using particle swarm optimization. It is important to note that both methods in [30], [31] and [35] require access to measured OSNR values, typically obtained via an Optical Spectrum Analyzer (OSA). Such measurements are generally not available in live transmission systems and are usually restricted to initial commissioning stages.

Table 1 Input parameter refinement techniques.

Ref. (band)	Main inputs and assumptions	Estimated Parameters
[30] (C)	Measured OSNR at OMS output	Insertion loss, amplifier noise figure spectrum
[31] (C)	Measured OSNR at OMS output, measured OMS output power spectrum, homogeneous rippled gain spectrum	Fiber parameters, insertion loss, average amplifier noise figure
[29] (C)	Measured output power spectrum at OMS	Insertion loss, amplifier gain spectrum
[18] (C+L)	Measured output power spectrum at OMS	Insertion loss, amplifier gain spectrum
[32] (C)	Measured output power spectrum at OMS, trained EDFA model	Insertion loss, amplifier gain spectrum
[33] (C+L)	Measured output power spectrum at each span, ripple-less gain spectrum	Insertion loss
[3] (C, C+L)	Measured output power spectrum at OMS, fully ASE-loaded system, calibrated full-load amplifier gain spectrum, possibility to adjust amplifier settings on-demand (the "active" part)	Insertion loss
[34] (C+L)	Measured output power spectrum at each span, fully ASE-loaded system	Insertion and splice loss
[35]	Measured input/output power spectrum at span with Raman amplifier	Output power spectrum with Raman amplifier
[IIR] (proposed, C)	Multi snapshots of measured output power spectrum at each OMS and service BER	Insertion loss, Amplifier gain spectrum, E2E offset noise

Our previous works [29], [18] leveraged OCMs, which provide per-channel optical power measurements at both the input and output of each Optical Multiplex Section (OMS), without the need for an OCM at each inline amplification site. In [29], we applied a gradient descent method to refine fiber insertion losses and amplifier gain spectra by minimizing the estimation error of the output power spectrum (measured by OCMs) in C-band networks, thereby enabling accurate QoT estimation. In [18], this approach was extended to C+L-band networks. By leveraging the stronger SRS effect in multi-band environments, we demonstrated that accurate insertion loss estimation is essential for prediction of Generalized SNR (GSNR), which accounts for ASE noise and Kerr nonlinearity but excludes transponder back-to-back noise. Consequently, GSNR can be evaluated at the OMS level. The study also showed that misestimation of insertion losses can result in large QoT prediction errors. In [32], fiber insertion loss refinement from [29] was combined with a neural network-based EDFA gain spectrum prediction model to predict the per-channel power variation when

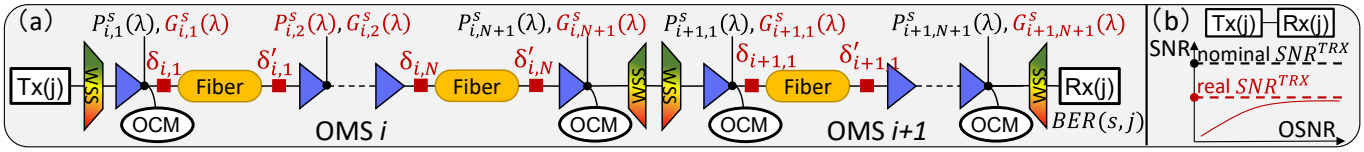

Fig. 1 (a) Topology of OMS-based optical network and its parameters; (b) Transponder back-to-back limit.

adding or dropping services; note that the new proposed parameter refinement technique in this paper could also be combined with advanced EDFA models as in [32] to improve the SNR prediction scenario. In [3], amplifier gain settings were actively adjusted to induce SRS-based power variation across spans. These variations were captured by OCMs and used to estimate per-span insertion losses and detect anomalies. However, this method depends heavily on the presence of a strong SRS effect and is therefore not well-suited to partial-load or low-load network scenarios. The method proposed in [33] assumes the availability of per-span OCMs and ripple-free gain spectra to enable accurate per-span insertion loss estimation. However, such assumptions are often unrealistic, and ignoring spectral ripple can lead to GSNR estimation errors of up to 1.5 dB. Similarly, the method in [34] localizes splice loss using SRS effects in full-load C+L systems, but accuracy depends heavily on device characterization, particularly EDFA gain spectra.

To address these limitations, we propose the IIR method. IIR leverages multiple network snapshots that contain OCM-measured power spectra (at the input and output of each OMS) and BER (SNR) measurements from the receivers. The method sequentially refines amplifier gain spectra, fiber insertion losses, and E2E offset noise (resulting from WSS filtering penalties and transponder variability). This approach enables autonomous QoT optimization in partially loaded C-band mesh networks, without requiring per-span OCM monitoring or idealized amplifier assumptions.

C. Contributions

We first introduced the IIR method in our OFC 2025 paper [36], where:

- The IIR algorithm was proposed and validated through simulation using experimental data from [16], based on a C-band ring-topology network. For the sake of completeness, we develop the algorithm in this paper, in Section 2.
- It was shown that the accuracy of fiber insertion loss estimation improves with the number of available snapshots, enabling enhanced QoT prediction and optimization. This is reported in Section 3.

This paper extends our previous work with the following new contributions, reported in Section 4 and Section 5:

- We propose a self-driven QoT optimization framework and experimentally validate the IIR method in a C-band mesh-topology network. The results show that IIR enables a multi-step, closed-loop optimization process, where each network reconfiguration (e.g., WSS adjustment) generates a new snapshot. These successive snapshots iteratively refine amplifier gain spectra, fiber insertion losses, and end-to-end offset noise, allowing the digital twin to become progressively more accurate and enhance the network margin. Execution-time and temporal-granularity analyses are also performed to assess computational scalability (Section 4).
- We provide a discussion of IIR's applicability and limitations in both offline and online modes, emphasizing its potential for real-time power optimization as well as challenges related to load-dependent amplifier dynamics, centralized computation, and runtime scalability (Section 5).

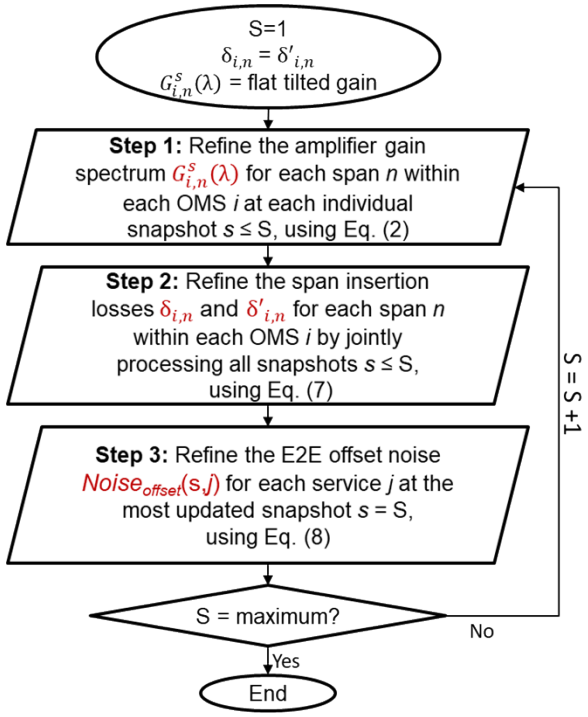

Fig. 2 Flow chart of the three-step IIR method.

Overall, this incremental refinement capability supports increasingly accurate and autonomous QoT optimization, enabling real-time decision-making in partially loaded mesh networks.

2. IIR METHOD DESCRIPTION

Fig. 1(a) shows the topology of an OMS-based optical network. The variables *s/j/i/n* represent the snapshot/service/OMS/span index, respectively. For example, in snapshot *s*, service *j* is transmitted by Tx(*j*) and received by Rx(*j*), passing through OMS *i*, with BER(*s,j*) monitored by Rx(*j*). The output power spectra at amplifiers *n=1* and *n=N+1* are monitored and known by OCM as $P^s_{i,1}(\lambda)$,$P^s_{i,N+1}(\lambda)$. We use the boldface notation for vectors and indicate wavelength-dependence and vector products are all element-wise.

The red parameters indicate unknown network parameters to be estimated by IIR, such as the (1) output power spectra of in-line amplifiers $P^s_{i,n}(\lambda)$, (2) gain spectra of all amplifiers $G^s_{i,n}(\lambda)$, and (3) the fiber insertion losses at the input/output $\delta_{i,n}/\delta'_{i,n}$ of each span. Note that (1) and (2) vary across network snapshots (states). The total uncertain insertion loss of each span ($\delta^{total}_{i,n} = \delta_{i,n} + \delta'_{i,n}$) is known and calculated as span loss minus fiber loss, where span loss is monitored by amplifier photodiodes, and fiber loss is calculated from fiber length and attenuation coefficient. Noise figure spectrum is assumed known from a lookup table for each amplifier. Additionally, the transponder b2b noise can be represented by SNR^{TRX}, which is the maximum achievable SNR in a b2b configuration, as shown in Fig. 1(b). We only know the nominal SNR^{TRX} from datasheets while the real

SNR^{TRX} is difficult to pre-calibrate since it depends on both Tx and Rx, and their pairing is unknown before deployment. Therefore, SNR^{TRX} is also treated as an unknown for each transponder pair (service). All the known and unknown parameters are fed into the DT.

The monitored BER can be converted into equivalent SNR, and subsequently into a Noise-to-Signal Ratio (NSR). The NSR of service *j* at snapshot *s*, denoted as $NSR(s,j)$, consists of multiple contributions:

$$NSR(s,j) = NSR^{ASE}(s,j) + NSR^{NLI}(s,j) + NSR^{TRX}(j) + FP(j) \quad (1)$$

Where:

- $NSR^{ASE}(s,j)$: noise from amplified spontaneous emission (ASE) generated by each amplifier along the service;
- $NSR^{NLI}(s,j)$: noise from fiber Kerr nonlinearity (NLI), influenced by the launch power spectrum per span;
- $NSR^{TRX}(j)$: transponder B2B noise;
- $FP(j)$: penalty due to WSS filtering.

The IIR method iteratively improves estimates of amplifier gain spectra, insertion losses, and residual noise offset through the three steps illustrated in Fig. 2.

Initialization

S denotes the index of the most recent network snapshot. In the initialization step, S = 1 corresponds to the initial network state. For each OMS i traversed by service j, the uncertain insertion loss for span *n* is initially split equally between the input and output of each span:

$$\delta_{i,n} = \delta'_{i,n}$$

The amplifier gain spectra are initially assumed to be linearly tilted.

Step 1: Gain Spectrum Refinement

For each individual snapshot $s \le S$, a gradient-descent algorithm [29] is applied to refine the amplifier gain spectra $G^s_{i,n}(\lambda)$, for each OMS i, assuming as a starting point that each span n has symmetric input and output losses ($\delta_{i,n} = \delta'_{i,n}$). The refinement starts from an initial linearly tilted gain spectrum and iteratively converges to minimize the discrepancy between the monitored and estimated power spectrum at the end of the OMS i:

$$Cost1 = \sqrt{\sum_\lambda \left[P^s_{i,N+1}(\lambda) - \widehat{P^s_{i,N+1}(\lambda)}\right]^2} \quad (2)$$

Where:

- $\boldsymbol{P^s_{i,N+1}}$ is the monitored power spectrum at the end of OMS i.
- $\widehat{\boldsymbol{P^s_{i,N+1}}}$ is the estimated spectrum at the end of OMS i after propagation from the first amplifier, including SRS, wavelength-dependent fiber attenuation, and the current gain profile estimate:

$$\widehat{\boldsymbol{P^s_{i,N+1}}} = \boldsymbol{P^s_{i,1}} \odot \prod_{n=1}^{N} (\delta_{i,n}\boldsymbol{\rho_{i,n}}(\boldsymbol{\alpha_{i,n}}, \boldsymbol{g_{i,n}}, \ldots)) \odot (\delta'_{i,n}\boldsymbol{G^s_{i,n}}) \quad (3)$$

Here, $\rho_{i,n}$ models the power evolution term including SRS effect (SRS coefficient $g_{i,n}$) and wavelength-dependent fiber attenuation (fiber attenuation coefficient $\alpha_{i,n}$). We apply the SRS triangular approximation model, which was experimentally validated in [38].

Step 2: Insertion Loss Refinement

The variation in NSR between snapshot *s* and a baseline snapshot (snapshot *k*) is defined as:

$$\Delta NSR(s,j) = NSR(s,j) - NSR(k,j) = \left(NSR^{ASE}(s,j) - NSR^{ASE}(k,j)\right) + \left(NSR^{NLI}(s,j) - NSR^{NLI}(k,j)\right) \quad (4)$$

Note that $NSR^{TRX}(j)$ and $FP(j)$ are assumed to be constant with time for each service *j* therefore they cancel out in Eq. (4).

The ASE and NLI components are calculated as follows:

$$NSR^{ASE}(s,j) = \sum_i \sum_{n=1}^{N+1} \frac{hfF^s_{i,n}(j)G^s_{i,n}(j)R_s}{P^s_{i,n}(j)} \quad (5)$$

$$NSR^{NLI}(s,j) = \sum_i \sum_{n=1}^{N+1} \gamma_{i,n}[P^s_{i,n}(j)]^2[\delta_{i,n}]^2 \quad (6)$$

Where:

- *h*: Planck's constant.
- *f*: Optical frequency of the service.
- $F^s_{i,n}(j)$ and $G^s_{i,n}(j)$: Noise figure and amplifier gain at the wavelength of service *j*, span *n*, OMS *i*, and snapshot *s*.
- $P^s_{i,n}(j)$: Optical power of service *j* at span *n*, OMS *i*, and snapshot *s*.
- R_s: baud rate.
- $\gamma_{i,n}$: nonlinear coefficent.

Once the gain spectra are refined, the ratio between the insertion loss $\delta_{i,n}$ and $\delta'_{i,n}$ is further refined for each span *n* within each OMS *i*, while maintaining a constant total uncertain loss $\delta^{\text{total}}_{i,n} = \delta_{i,n} + \delta'_{i,n}$. This refinement is performed using a gradient-descent method "L-BFGS-B" [41], by minimizing the following cost function Cost2, jointly considering all snapshots $s \le S$:

$$Cost2 = \sqrt{\sum_s \sum_j \left[\Delta NSR(s,j) - \widehat{\Delta NSR(s,j)}\right]^2} \quad (7)$$

Since booster launch power spectrum changes over snapshots, both $NSR^{ASE}(s,j)$ and $NSR^{NLI}(s,j)$ are snapshot-dependent, which we account for. In contrast, we neglect the variation of $NSR^{TRX}(j)$ and $FP(j)$ and assume constant noise across snapshots.

This sequential process consists of gain spectrum refinement followed by insertion loss refinement. It is designed because the gain refinement relies solely on power modeling (see *Cost1*), whereas the insertion loss refinement relies on SNR modeling across all services and snapshots (see *Cost2*). Performing gain refinement first ensures correct power propagation along the OMSs, enabling reliable SNR estimation with the subsequent insertion loss refinement. Instead of iterative back-and-forth refinements between the two steps, this order avoids feedback between gain and loss updates, reducing computational complexity while maintaining adequate modeling accuracy.

Step 3: E2E Offset Noise Refinement

This step compensates for any residual modeling mismatch that remains after the refinement of insertion losses (Step 1) and amplifier gain spectra (Step 2).

For each service *j* at snapshot *s*, the E2E offset noise is defined as the error between the monitored and estimated NSR (with Step 1 and 2):

$$Noise_{offset}(s,j) = \varepsilon^{est}_{before\ Step\ 3}(s,j) = NSR(s,j) - \widehat{NSR(s,j)} \quad (8)$$

Where:

- $NSR(s,j)$ is the monitored NSR derived from the measured BER of service j at snapshot *s*.
- $\widehat{NSR(s,j)}$ is the estimated NSR of service j at snapshot *s* after refinement of insertion loss $\delta_{i,n}, \delta'_{i,n}$ (from Step 1) and amplifier gain spectrum $\boldsymbol{G^s_{i,n}}$ (from Step 2), obtained using data from previous snapshots $[1,\ldots,s-1]$.
- $\varepsilon^{est}_{before\ Step\ 3}(s,j)$ represents the residual estimation error of NSR before applying Step 3.

This offset term accounts for residual impairments not fully captured by the physical models implemented in the digital twin, such as transponder B2B noise and WSS-induced filtering penalties.

At the most recent snapshot (s = S), the offset term is calibrated so that the modeled NSR, including the offset correction, exactly matches the monitored NSR. By construction, the residual estimation error at snapshot $s = S$ is eliminated:

$$\varepsilon^{est}_{after\ Step\ 3}(s = S,j) = \left[\widehat{NSR(s = S,j)} + Noise_{offset}(s = S,j)\right] - NSR(s = S,j) = 0 \quad (9)$$

The calculated $Noise_{offset}(s = S,j)$ is then reused to correct the future prediction of NSR (SNR) at snapshot s = S+1, thereby reducing the prediction error:

$$\varepsilon^{pred}_{after\ Step\ 3}(s = S+1,j) = \left[\widehat{NSR(s = S+1,j)} + Noise_{offset}(s = S,j)\right] - NSR(s = S+1,j) \quad (10)$$

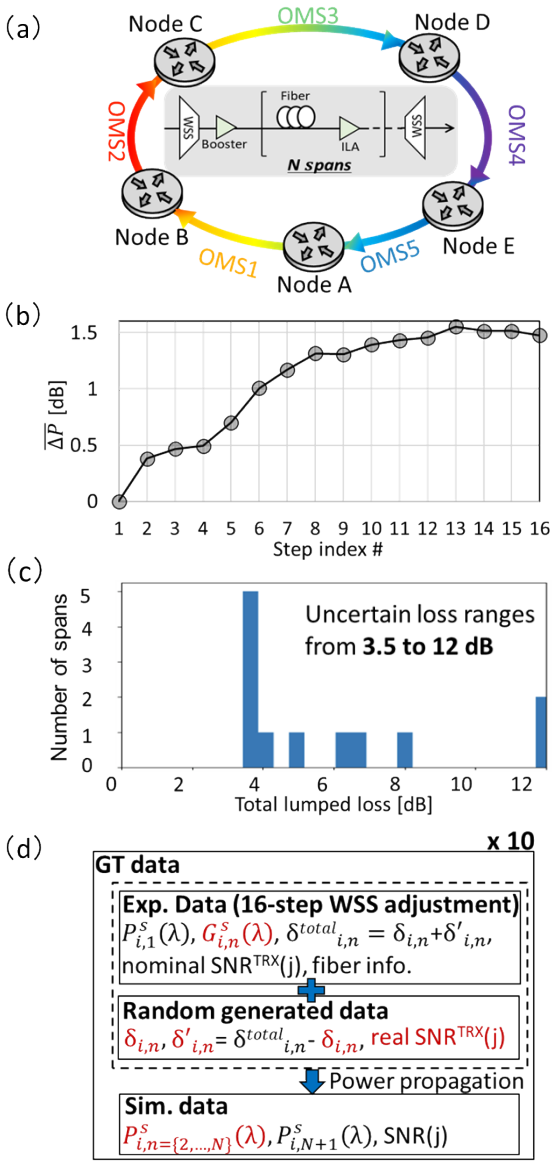

Fig. 3 (a) 5-OMS ring-topology network; (b) Average booster power variation across snapshots; (c) Histogram of total uncertain insertion loss across all spans; (d) Data usage assumption for simulation validation.

3. SIMULATION VALIDATION FOR IIR

A. Simulation Testbed

The proposed IIR method was first validated through simulations using experimental data gathered in the experiment described in [16]. The experimental dataset includes 15 steps (16 snapshots in total, including the initial snapshot) of WSS adjustments in a C-band ring-topology network to optimize power profiles. The testbed, illustrated in Fig. 3(a), consists of 5 OMSs with heterogeneous fiber lengths and types; 12 routing paths are configured, with additional OMS details provided in **Table 2** and service routing information in **Table 3**. Each routing path carries five services traversing between 1 and 4 OMSs, for a total of 60 services using 90 Gbaud 400G PCS-16QAM modulation. At each step, WSS reconfiguration modifies the attenuation of multiple channels (up to 1 dB per channel) on a single OMS, thereby altering its booster power

Table 2 OMS info.

Item	OMS1	OMS2	OMS3	OMS4	OMS5
Number of spans	2	2	5	2	1
Span details	40+80 km LEAF	80+20 km SMF	5x80 km SMF	80 km LEAF + 80 km TW	20 km SMF
Total length	120 km	100 km	400 km	160 km	20 km
# channels	30	35	45	40	30
Channel information	400 Gb/s (90 Gbaud, PCS16QAM) transponder, 100 GHz grid in the 6 THz C-band.				

Table 3 Routing table.

Source	Sink	Path	Service #
C	B	3-4-5-1	5
B	A	2-3-4-5	5
A	E	1-2-3-4	5
D	C	4-5-1-2	5
C	A	3-4-5	5
C	E	3-4	5
B	E	2-3-4	5
D	B	4-5-1	5
A	D	1-2-3	5
B	D	2-3	5
E	C	5-1-2	5
C	D	3	5

spectrum. Fig. 3(b) shows the average (taken over all channels used by a service) booster power variation across the M=5 OMSs for all 16 snapshots, denoted as $\overline{\Delta P}$:

$$\overline{\Delta P}(s) = \frac{1}{M}\sum_{i=1}^{M} |P^{s}_{i,1}(:) - P^{1}_{i,1}(:)| \quad (11)$$

Additional implementation details for the underlying experimental dataset can be found in [16].

As shown in Fig. 3(d), we generate 16 network snapshots using a combination of experimental and randomly generated data. The experimental data include:

- Booster power spectra $P^{s}_{i,1}$ from each WSS step;
- Amplifier gain spectra $G^{s}_{i,n}(\lambda)$;
- Total insertion losses $\delta^{total}_{i,n}$ (ranging from 3.5 to 12 dB, also shown in Fig. 3(c));
- Nominal transponder B2B ceiling SNR: SNR^{TRX};
- Fiber characteristics.

The randomly generated data include:

- Insertion loss at input of each fiber: $\delta_{i,n}$ from U[0,3] dB
- Insertion loss at output of each fiber: $\delta'_{i,n} = \delta^{total}_{i,n} - \delta_{i,n}$
- Real B2B transponder ceiling SNR with added uncertainty for each service: SNR^{TRX} + (unknown) U[-1,1] dB

The generated insertion losses $\delta_{i,n}$, $\delta'_{i,n}$ and the uncertain transponder ceiling SNR are kept constant across all 16 snapshots to emulate stable hardware conditions. For each snapshot, the booster power spectrum $P^{s}_{i,1}(\lambda)$ is propagated along the OMS to compute the output spectra of intermediate and pre amplifiers $P^{s}_{i,n}(\lambda)$, n = 2,…,N + 1. The SNR of each service is then calculated using the Gaussian noise model [27].

All experimental, random, and simulated parameters are treated as ground truth (GT) to construct the 16 snapshots. The proposed IIR algorithm is then applied to estimate the unknown parameters (highlighted in red in Fig. 1), using only the known parameters (in black in Fig. 1) from the generated snapshots. We use the initial snapshot as the baseline snapshot (k=1 in Eq. (4)).

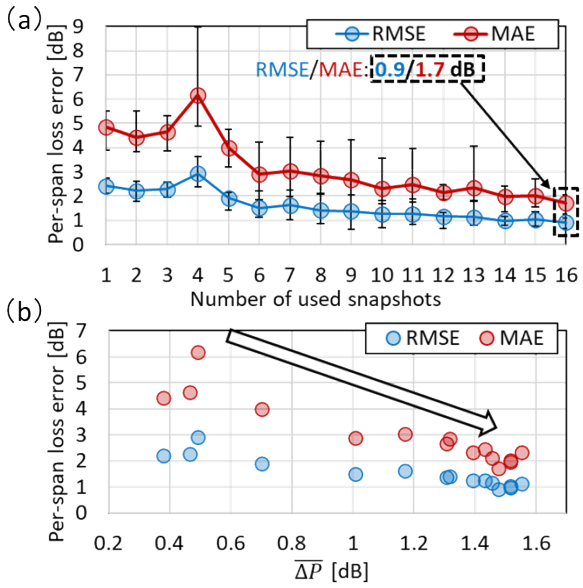

Fig. 4 (a) Per-span insertion loss estimation accuracy; (b) Correlation between insertion loss estimation accuracy and power variation;

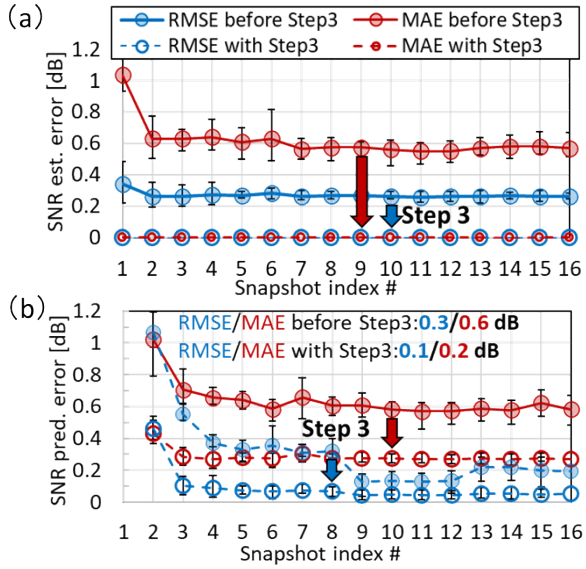

Fig. 5 (a) SNR estimation with IIR; (b) SNR prediction with IIR.

To statistically validate the IIR method in simulation, we generate 10 independent test cases. Across all cases, the booster power spectra, amplifier gain spectra, total insertion losses, and fiber characteristics remain identical. The differences among the test cases arise from the randomly generated per-span insertion losses, per-service B2B transponder ceiling SNRs including random uncertainty, and the resulting output spectra of intermediate and pre-amplifiers as well as the service SNRs obtained by propagating the booster power spectra through the corresponding insertion losses and amplifier gain spectra. Each test case, consisting of 16 snapshots, is processed independently by the IIR algorithm, and the resulting estimations are averaged. The robustness and consistency of the proposed method are then evaluated using root-mean-square error (RMSE) and maximum absolute error (MAE) bars across the 10 cases.

B. Simulation Results

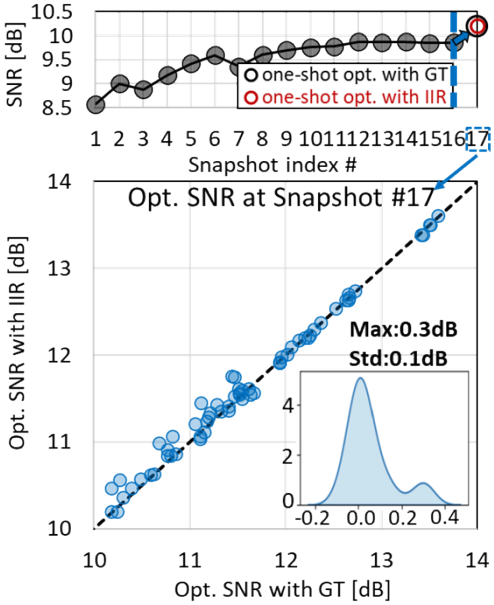

Fig. 6 Optimized network margin (top) and one-shot optimized SNR (bottom).

1. Insertion Loss Estimation

Fig. 4(a) shows the accuracy of per-span insertion loss refinement using IIR as a function of the number of utilized snapshots. Both root-mean-square error (RMSE) and maximum absolute error (MAE) are reported. Each data point represents the average of 10 randomized test cases, and the error bars indicate the range. At snapshot #1, the initial assumption $\delta_{i,n} = \delta'_{i,n}$ yields an RMSE and MAE of 2.4 dB and 4.8 dB, respectively. With only a few snapshots (e.g., 4), the MAE increases to 6.2 dB due to insufficient variation to be learned, hence hindering proper parameter estimation and thus causing large error. As more snapshots are collected, IIR significantly improves the connector loss accuracy, reducing the error to 0.9 dB RMSE and 1.7 dB MAE when using all 16 snapshots.

Fig. 4(b) shows the correlation between fiber insertion loss estimation error and average booster power variation $\overline{\Delta P}$ (shown in Eq. (11)). As the power variation and the associated SRS and BER variations increase, insertion loss estimation improves. With average power variation reaching approximately 1.5 dB, the RMSE converges to 0.9 dB.

2. QoT Estimation and Prediction

Fig. 5(a) reports the estimated SNR at snapshot *s*, using IIR-refined parameters from snapshots #1 to *s* as input to the DT. At snapshot #16, the error remains at 0.3 dB RMSE and 0.6 dB MAE, mainly due to the uncertainty of the E2E offset noise. In Step 3 of IIR, this E2E offset is estimated and used to correct the SNR estimation error, which is reduced to zero by construction. As shown later, this offset correction enables highly accurate SNR prediction. Fig. 5(b) presents the SNR predicted at snapshot *s* using IIR-refined parameters from snapshots #1 to *s-1*. Without the offset correction, the prediction error at snapshot #16 is 0.3 dB RMSE and 0.6 dB MAE. When the refined offset noise from Step 3 is included, the error decreases to 0.1 dB RMSE and 0.2 dB MAE. The remaining error is due to imperfections in parameter refinement and unmodeled changes in amplifier gain spectra.

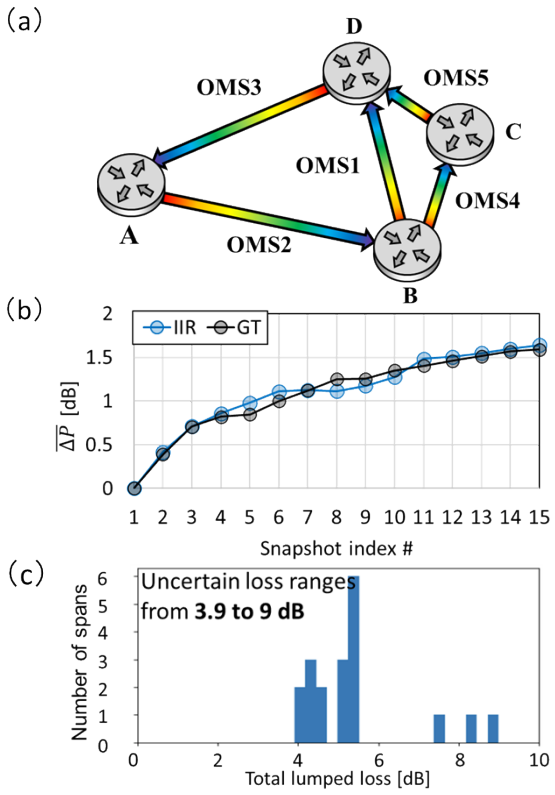

Fig. 7 (a) 5-OMS mesh network; (b) Average booster power variation; (c) Histogram of total uncertain insertion losses.

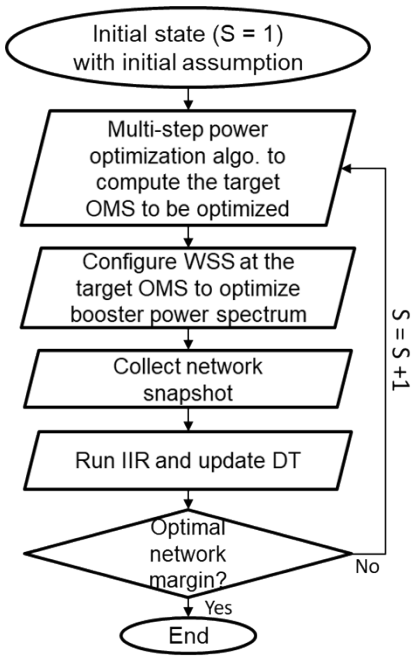

Fig. 8 Flow chart of the IIR-enabled closed-loop multi-step power optimization.

3. One-shot QoT Optimization

Fig. 6 (top) shows the network margin (i.e., the worst-case SNR among all services) during the 15-step WSS-based power optimization, using GT parameters from snapshots #2 to #16 (black dots, left of the blue dashed line). At snapshot #16, a further one-shot power optimization is performed by adjusting the launch power spectrum of the booster of each OMS for snapshot #17 using DT-based targets to achieve ASE/NLI equal to 3 dB for each service at the output of each OMS, as suggested by the LOGO strategy [26]. The optimization is performed with either GT parameters (black circle at snapshot #17) or IIR (red circle)-refined parameters. In both cases, the network margin increases from 9.8 dB to 10.2 dB, indicating that IIR-refined parameters are sufficiently accurate for optimization.

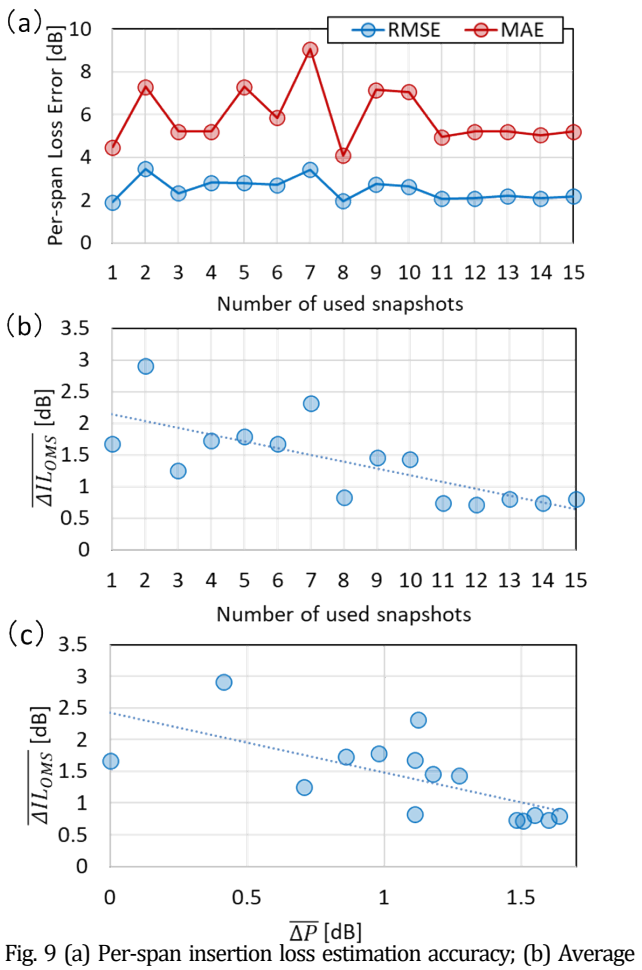

Fig. 9 (a) Per-span insertion loss estimation accuracy; (b) Average absolute error of OMS-level insertion loss estimation; (c) Correlation between OMS-level insertion loss estimation accuracy and power variation.

Fig. 6 (bottom) compares DT-optimized SNRs for all 60 services at snapshot #17 using IIR-refined versus GT parameters. The inset shows the probability density function of the SNR difference. The results confirm close agreement, with a standard deviation of 0.1 dB and a maximum difference of 0.3 dB.

4. EXPERIMENTAL VALIDATION FOR IIR

To evaluate the robustness of the proposed IIR method under realistic network conditions, the experimental validation was designed to inherently account for measurement and modeling uncertainties rather than relying on idealized conditions. These uncertainties include power measurement errors, SNR estimation noise, and DT modeling inaccuracies such as analytical-model inaccuracy (e.g., SRS, ASE noise, and nonlinear interference modeling) and uncertain parameters (e.g., NF spectra and real transponder B2B SNR^{TRX}).

A. Experimental Testbed

Table 4 OMS info.

Item	OMS1	OMS2	OMS3	OMS4	OMS5
Number of spans	5	5	5	2	2
Span details	5x80 km SMF	5x100 km PSCF	2*100 km PSCF+60/ 80/100 km SMF	80 km LEAF+80 km TW	40 + 80 km SMF
Total length	400 km	500 km	440 km	160 km	120 km
# channels	30	50	50	30	30
Channel information	400 Gb/s (90 Gbaud, PCS16QAM) transponder,100 GHz grid in the 6 THz C-band.				

Table 5 Routing table.

Source	Sink	Path	Service #
B	D	1	10
B	A	1-3	10
A	D	2-1	10
A	C	2-4	5
D	B	3-2	5
D	C	3-2-4	15
B	C	4	10
C	D	5	10
C	A	5-3	5
C	B	5-3-2	15

The proposed IIR method was experimentally validated in a 5-OMS mesh-topology network, shown in Fig. 7(a). The details of the testbed configuration are provided in **Table 4**. It consists of 5 OMSs with heterogeneous fiber types (i.e., SMF, PSCF, LEAF, and TW) and span lengths ranging from 40 km to 100 km. **Table 5** summarizes the 10 routing paths configured in the network. Each path carries between 5 and 15 services, traversing 1 to 3 OMSs, for a total of 95 services in this partially loaded C-band network. Channel loading is emulated using an ASE source, and the BER (and corresponding SNR) is measured using a real-time transponder operating at 90 Gbaud with 400G PCS-16QAM modulation, which remains the same across all measurements. Transponder B2B SNR^{TRX} is characterized in the lab.

Similarly to the simulation validation, each individual transponder (service) in the experiment is assigned a (unknown) uniformly distributed variation of U[-1,1] dB in its nominal B2B SNR^{TRX}, reflecting realistic uncertainty due to transceiver performance differences and pairing mismatch. In addition, a flat NF spectrum is assumed across all wavelengths, obtained from a lookup table corresponding to the nominal gain setting of each amplifier. This assumption, while different from the realistic wavelength-dependent and rippled NF spectra observed in deployed systems, reflects the practical uncertainty of NF characterization in real networks, where detailed NF measurements are typically unavailable, especially under partial-load conditions.

This experiment focuses on an automated closed-loop QoT optimization framework based on a DT, whose architecture is shown in Fig. 8. The objective is to maximize the network margin (the worst-case SNR among all services), using a multi-step power optimization algorithm adapted from [11]. At each optimization step, the algorithm selects a target OMS for WSS reconfiguration, based on the predicted improvement to the network margin. The WSS attenuation profile of selected channels is modified by up to 1 dB per channel, altering the booster power spectrum of the selected OMS. The average booster power variation across all five OMSs $\overline{\Delta P}$ (shown in Eq. (11)) over the 14 optimization steps with 1) GT parameters and 2) IIR-refined parameters are shown in Fig. 7(b). Fig. 7(c) shows the total insertion losses $\delta_{i,n}^{total}$, ranging from 3.9 to 9 dB.

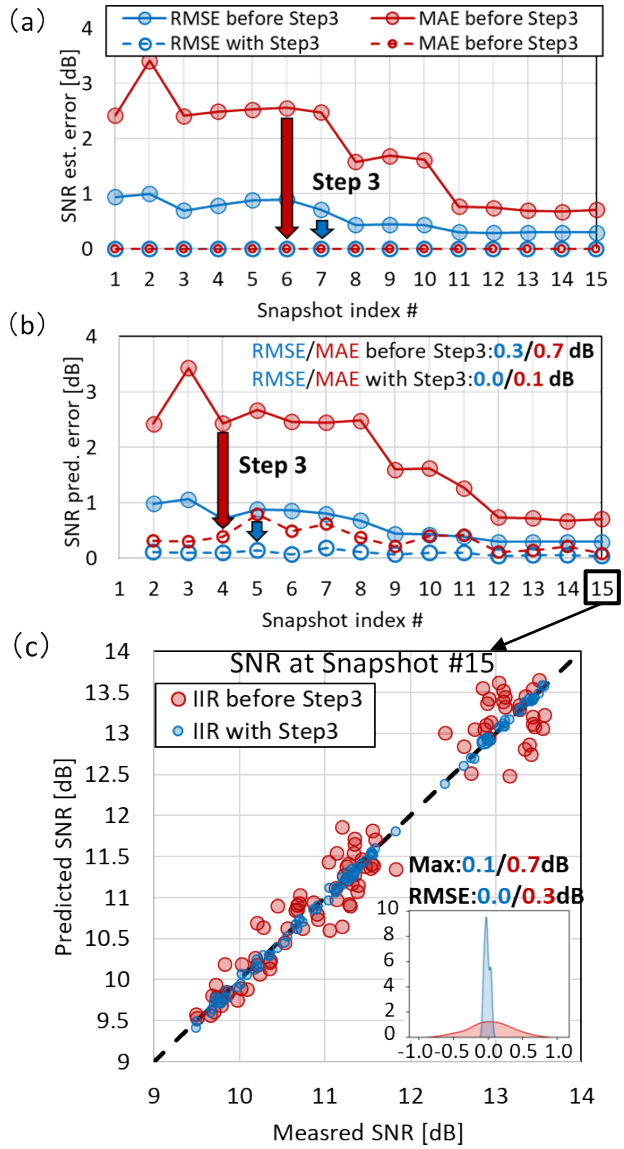

Fig. 10 (a) SNR estimation with IIR; (b) SNR prediction with IIR; (c) SNR prediction accuracy with/without IIR step 3 at Snapshot #15.

The OMS selection and attenuation control rely entirely on the accuracy of QoT predictions enabled by the DT, which in turn depend on the accuracy of its input parameters. To ensure accurate input parameter refinement, a new network snapshot is collected after each WSS adjustment, and the IIR method is applied using all accumulated snapshots, enabling incremental refinement of fiber insertion losses, amplifier gain spectra, and E2E offset noise. These refined parameters are used to update the DT model, allowing progressively improved QoT prediction and more effective decision-making at each step of the optimization process to improve the network margin.

B. Experimental Results

1. Insertion Loss Estimation

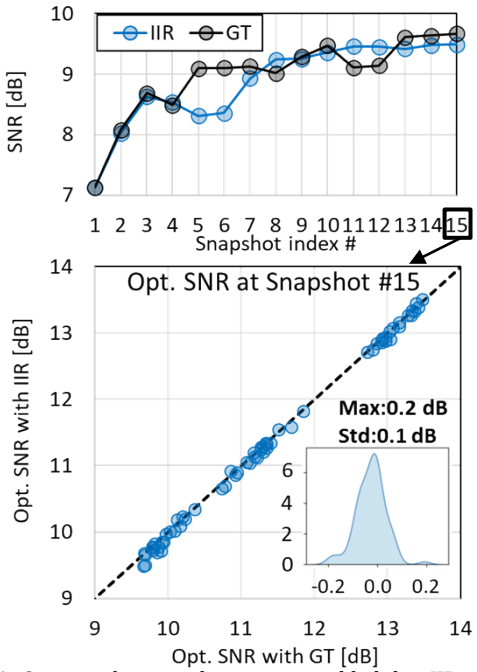

Fig. 11 Optimized network margin enabled by IIR-refined/GT parameters (top), and optimized SNR at snapshot #15 (bottom).

Fig. 9(a) shows the accuracy of per-span insertion loss refinement using IIR across different numbers of snapshots. Both RMSE and MAE do not show improvement with additional snapshots: the initial 50%/50% insertion loss split assumption yields an RMSE/MAE of 1.9/4.5 dB, while IIR using 15 snapshots results in slightly worse values of 2.2/5.2 dB. This degradation is primarily due to modeling inaccuracies such as SRS and Kerr effects, which limit the accuracy of per-span estimation. In contrast, simulation results in Section 3 show improved accuracy under idealized conditions without such modeling uncertainties. Fig. 9(b) shows the average absolute error of per-OMS insertion loss estimation across M=5 OMSs, as defined by:

$$\overline{\Delta IL_{OMS}} = \frac{1}{M}\sum_{i=1}^{M} |\overline{IL_i^{IIR}}|, \quad (12)$$

where the average insertion loss per OMS is given by:

$$\overline{IL_i^{IIR}} = \frac{1}{N}\sum_{n=1}^{N}(IL_{i,n}^{IIR} - IL_{i,n}^{GT}). \quad (13)$$

The results show that while per-span insertion loss estimation remains inaccurate, IIR significantly improves insertion loss estimation at the OMS level. With 15 snapshots, the average OMS-level insertion loss error is reduced from 1.7 dB to 0.7 dB. This improvement is due to IIR's ability to aggregate the effects over multiple spans, thereby mitigating modeling inaccuracies. Since the impact of insertion loss on QoT, primarily through Kerr nonlinearity, depends on the characteristics of each span, it is possible to achieve accurate SNR estimates even if individual span losses are inaccurate, as long as their cumulative nonlinear effect is preserved. In contrast, the initial 50/50% split often results in incorrect aggregate impact. In summary, IIR refines insertion losses so that QoT estimation or prediction remains globally accurate at the OMS and service levels, despite local per-span errors.

Fig. 9(c) illustrates the correlation between the average OMS-level insertion loss estimation error and the average booster power variation $\overline{\Delta P}$ across 5 OMSs between snapshot s and snapshot #1. The results indicate that greater power variation, and consequently greater BER (SNR) variation, leads to more accurate insertion loss estimation. When the average power variation reaches 1.6 dB, the OMS-level insertion loss error is reduced from 1.7 dB to 0.7 dB.

2. QoT Estimation and Prediction

Fig. 10(a) reports the estimated SNR at snapshot s, using IIR-refined parameters from snapshots #1 to s as input to the DT model. At snapshot #15, the error remains 0.3 dB RMSE and 0.7 dB MAE, a substantial improvement compared to the initial state using the default parameter assumptions, where the RMSE and MAE are 0.9 dB and 2.4 dB, respectively. This demonstrates that, although per-span insertion loss estimation remains inaccurate, IIR significantly improves OMS-level insertion loss estimation, thereby enhancing the accuracy of nonlinear impairment modeling. The remaining error is primarily attributed to the uncertainty in the E2E offset noise. In Step 3 of the IIR process, this E2E offset is estimated and used to correct the NSR error, effectively reducing the error to zero (by construction).

Fig. 10(b) presents the SNR predicted at snapshot s using IIR-refined parameters from snapshots #1 to s-1. Without offset correction (Step 3; red disks), the prediction error is improved from 1.0 dB RMSE and 2.4 dB MAE at initial state to 0.3 dB RMSE and 0.7 dB MAE for snapshot s=15. When the refined offset noise from Step 3 is incorporated (blue disks), the error is further reduced to <0.1 dB RMSE and 0.1 dB MAE. These results demonstrate that IIR enables highly accurate QoT prediction by progressively refining physical-layer parameters and compensating for E2E offset noise contributions.

Fig. 10(c) presents the predicted SNR using IIR-refined parameters, with and without the application of Step 3 (E2E offset noise refinement). The results are consistent with those shown in Fig. 10(b) at snapshot #15. Before applying Step 3, the prediction exhibits an RMSE/MAE of 0.3/0.7 dB. After Step 3 is applied, the prediction accuracy significantly improves, reducing the error to below 0.1 dB for both RMSE and MAE. The inset displays the probability density function of the SNR prediction error, confirming the improved prediction accuracy achieved through E2E offset noise refinement.

3. IIR-enabled Multi-step QoT Optimization

Fig. 11 (top) shows the network margin (worst-case SNR) among all 95 services at different snapshots during the multi-step optimization process, using either 1) GT or 2) IIR-refined parameters. With GT parameters, the margin increases from 7.1 dB to 9.7 dB, while IIR-refined parameters yield an improvement from 7.1 dB to 9.5 dB. This small 0.2 dB difference confirms that the IIR-refined parameters are sufficiently accurate to enable effective QoT optimization, achieving near-identical performance to the GT case.

Fig. 11 (bottom) compares the optimized SNRs for all 95 services at snapshot #15 using IIR-refined versus GT parameters. The inset shows the probability density function of the SNR differences. The results demonstrate strong agreement, with a standard deviation of 0.1 dB and a maximum deviation of 0.2 dB.

4. Temporal Granularity and Execution Time Analysis

To complement the performance evaluation, we assess the temporal granularity and execution time of each step in the IIR-enabled QoT optimization process. The interval between two consecutive snapshots involves four procedures: (i) acquisition of a new snapshot, (ii) digital-twin–based IIR refinement using all previous snapshots, (iii) digital-twin–based multi-step power optimization, and (iv) WSS reconfiguration. Note that only (i) and (ii) pertain to IIR while (iii) and (iv) pertain to the QoT optimization process.

In the experimental setup, SNR measurement required about four hours to cover all 95 services, as only one commercial transponder was available and measurements were performed sequentially. In practical networks, parallel measurements across multiple transponders could reduce snapshot acquisition time to the second timescale.

The multi-step power optimization operates on the minute timescale, while the IIR algorithm requires about 10 minutes on a standard computer with 2 snapshots and up to one hour with 15 snapshots. The

most time-consuming task is Step 2 of IIR, which uses gradient descent to refine per-span insertion losses while computing SNRs across all snapshots. This can be accelerated by refining OMS-level average losses instead of per-span values, since results show that most accuracy gains occur at the OMS level. This simplification reduces the number of refined parameters from 19 spans to 5 OMSs without compromising QoT estimation accuracy and can be explored in future work.

Finally, the WSS configuration time is on the order of seconds, which could be reduced to less than 50 ms using fast WSS as demonstrated in [42]. Overall, although the full IIR process with many snapshots may take up to one hour, it can be further optimized by refining average OMS-level insertion losses instead of per-span values, which can be investigated in future work.

5. APPLICATION SCENARIOS AND LIMITS

The proposed IIR method can be applied in two modes:

- **Offline mode**: using multiple historical network snapshots to refine physical-layer parameters for future SNR prediction and optimization;
- **Online mode**: integrating IIR within a multi-step network reconfiguration process, thus enabling a closed-loop optimization of SNR prediction and power settings.

A key assumption of IIR is that the insertion losses remain constant across the selected snapshots. Therefore, snapshots should be collected within a relatively short time window to ensure stable losses, as they may other wise fluctuate due to human-induced effects (e.g., dirty connectors or fiber splices after repairs).

In this paper, we demonstrate that IIR performs well in power re-optimization scenarios with constant channel loading. Under load-varying conditions, however, amplifier gain and NF spectra may change due to load-dependent dynamics, reducing accuracy. While gain spectra can still be refined independently at each snapshot (Step 1), NF variations cannot be directly monitored in commercial networks [30]. This unobserved variation in NF and consequently in $\mathrm{NSR}^{\mathrm{ASE}}$ can be absorbed into variations of $\mathrm{NSR}^{\mathrm{NLI}}$ (see Eq. (4)), leading to an inaccurate tracking of $\mathrm{NSR}^{\mathrm{NLI}}$ variations among snapshots, and consequently degrading the accuracy of insertion loss estimation. A possible mitigation is to calibrate NF spectra using lookup tables that account for loading, nominal gain, and total output power, hence improving the estimation of both $\mathrm{NSR}^{\mathrm{ASE}}$ and $\mathrm{NSR}^{\mathrm{NLI}}$, leading to more accurate refined insertion losses.

Another limitation concerns the data acquisition and computational architecture of the IIR process. The refinement of insertion losses, amplifier gain spectra, and E2E offset noise requires network-wide information across all services, meaning that data from multiple OMSs must be collected and jointly processed. As a result, the IIR algorithm can be performed in a centralized manner, since each individual OMS lacks information about services traversing other OMSs. This centralized design limits time efficiency and scalability for large networks, as distributed, per-OMS implementations are not yet feasible without global network awareness. Future work will investigate distributed or hierarchical implementations of IIR to improve scalability and real-time applicability.

Moreover, as mentioned in Section 4-B.4, the computation time of IIR also needs improvement. Refining average OMS-level insertion losses instead of per-span values can greatly reduce runtime while preserving QoT estimation accuracy.

In summary, IIR can be effectively used offline for parameter refinement and future SNR prediction, and online for real-time power optimization. It achieves high accuracy under stable loading and insertion-loss conditions but is challenged by dynamic loading, centralized computation, and hour-scale runtime. Future work will focus on adaptive, load-aware modeling and distributed implementations for scalable and robust SNR prediction in reconfigurable optical networks.

6. CONCLUSION

We proposed a novel technique, IIR, that leverages multiple network snapshots to iteratively refine amplifier gain spectrum, fiber insertion loss, and E2E service offset noise. This approach enables accurate QoT prediction and efficient self-driven QoT optimization in optical networks. The IIR method was validated through both simulations (based on experimental data on a C-band ring-topology network with 5 OMSs), and experiments on a C-band mesh-topology network with 5 OMSs. Results demonstrate that IIR significantly improves insertion loss estimation, QoT prediction accuracy, and optimization performance, achieving near-identical performance to the case knowing GT parameters. These findings highlight the critical importance of accurate physical-layer parameter estimation for the performance and reliability of modern optical networks. By effectively exploiting monitored data across multiple network snapshots, the proposed IIR method offers a practical and scalable solution to address uncertainties arising from nonlinear effects and hardware variability. It lays a foundation for robust and autonomous optical network control, well-aligned with the stringent performance and flexibility demands of emerging 5G and 6G infrastructures.

References

1. X. Yang, A. Ferrari, D. Le Gac, G. Charlet, M. Tornatore, and Y. Pointurier, "Experimental impact of power re-optimization in a mesh network," J. Opt. Commun. Netw. 15, C20-C28 (2023).
2. X. Liu, Q. Qiu, Y. Zhang, M. Cai, Y. Liu, L. Yi, W. Hu, and Q. Zhuge, "Auto-DTWave: Digital Twin-Aided Autonomous Optical Network Operation with Continuous Wavelength Loading," in Optical Fiber Communications Conference and Exhibition (OFC) (2024), paper Th1G.5.
3. X. Yang, C. Sun, G. Charlet, M. Tornatore, and Y. Pointurier, "Digital-twin-based active input refinement for insertion loss estimation and QoT optimization in C and C + L networks," J. Opt. Commun. Netw. 16, 1261-1274 (2024).
4. X. Liu, Q. Qiu, Y. Zhang, Y. Cheng, L. Yi, W. Hu, and Q. Zhuge, "First Field Trial of LLM-Powered AI Agent for Lifecycle Management of Autonomous Driving Optical Networks," in Optical Fiber Communication Conference (OFC) 2025, paper Th1A.2.
5. K. Christodoulopoulos, C. Delezoide, N. Sambo, A. Kretsis, I. Sartzetakis, A. Sgambelluri, N. Argyris, G. Kanakis, P. Giardina, G. Bernini, D. Roccato, A. Percelsi, R. Morro, H. Avramopoulos, P. Castoldi, P. Layec, and S. Bigo, "Toward efficient, reliable, and autonomous optical networks: the ORCHESTRA solution [Invited]," J. Opt. Commun. Netw. 11, C10-C24 (2019).
6. C. Sun, X. Yang, N. Di Cicco, R. Ayassi, V. Virajit Garbhapu, P. A. Stavrou, M. Tornatore, G. Charlet, and Y. Pointurier, "Experimental demonstration of local AI-Agents for lifecycle management and control automation of optical networks," J. Opt. Commun. Netw. 17, C82-C92 (2025).
7. V. V. Garbhapu, A. Ferrari, I. F. de Jauregui Ruiz, D. Le Gac, G. Charlet and Y. Pointurier, "Network-Wide SNR-based Channel Power Optimization," in European Conference on Optical Communication (ECOC) (2021), paper Tu2E.5.
8. G. Borraccini, A. D'Amico, S. Straullu, F. Usmani, A. Ahmad, and V. Curri, "Iterative supervised learning approach using transceiver bit-error-rate measurements for optical line system optimization," J. Opt. Commun. Netw. 15, 111-118 (2023).

9. A. Ferrari, D. Pilori, E. Virgillito, and V. Curri, "Power Control Strategies in C+L Optical Line Systems," in Optical Fiber Communications Conference and Exhibition (OFC) (2019), paper W2A.48.
10. I. Roberts, J. M. Kahn and D. Boertjes, "Convex Channel Power Optimization in Nonlinear WDM Systems Using Gaussian Noise Model," J. Lightwave Technol. 34, 3212-3222 (2016).
11. C. Sun, X. Yang, G. Charlet, P. A. Stavrou, and Y. Pointurier, "Digital twin-enabled multi-step strategies for autonomous power equalization in optical networks," J. Opt. Commun. Netw. 17, C41-C50 (2025).
12. D. Wang, Y. Song, Y. Zhang, X. Jiang, J. Dong, F. Khan, T. Sasai, S. Huang, A. Pak Tao Lau, M. Tornatore, M. Zhang, "Digital Twin of Optical Networks: A Review of Recent Advances and Future Trends," J. Lightwave Technol. 42, 4233-4259 (2024).
13. M. S. Faruk and S. J. Savory, "Measurement informed models and digital twins for optical fiber communication systems," J. Lightw. Technol., 42, 1016–1030 (2024).
14. A. Ferrari, K. Balasubramanian, M. Filer, Y. Yin, E. Le Rouzic, J. Kundrat, G. Grammel, G. Galimberti, and V. Curri, "Assessment on the in-field lightpath QoT computation including connector loss uncertainties," J. Opt. Commun. Netw. 13, A156–A164 (2021).
15. Y. Pointurier, "Design of low-margin optical networks," J. Opt. Commun. Netw. 9, A9-A17 (2017).
16. C. Sun, X. Yang, G. Charlet, P. A. Stavrou, and Y. Pointurier, "Digital Twin-Enabled Optical Network Automation: Power Re-Optimization," in Optical Fiber Communication Conference (OFC) (2024), paper W4I.5.
17. X. Yang, C. Sun, G. Charlet, M. Tornatore, and Y. Pointurier, "Digital Twin-based Insertion Loss Estimator for Anomalous Loss Localization and Network Equalization Enhancement," in Optical Fiber Communication Conference (OFC) (2024), paper W4I.4.
18. X. Yang, A. Ferrari, N. Morette, et al., "QoT estimation improvement with inputs refinement tool for C+ L networks," in Optical Fiber Communication Conference (OFC) (2023), paper W4G.6.
19. R. Yang, S. Shen, H. Li, Z. Shi, R. Wang, R. Nejabati, S. Yan, and D. Simeonidou, "986 km field trial of cascaded ANN-based link penalty models for QoT prediction," in Optical Fiber Communication Conference (OFC) (2023), paper W4G.5.
20. Z. Wang, Y. -K. Huang, S. Han, T. Wang, D. Kilper and T. Chen, "Multi-Span Optical Power Spectrum Prediction using ML-based EDFA Models and Cascaded Learning," in Optical Fiber Communication Conference (OFC) (2024), paper M1H.6.
21. R. M. Morais and J. Pedro, "Machine learning models for estimating quality of transmission in DWDM networks," J. Opt. Commun. Netw. 10, D84–D99 (2018).
22. C. Rottondi, L. Barletta, A. Giusti, and M. Tornatore, "Machine-learning method for quality of transmission prediction of unestablished lightpaths," J. Opt. Commun. Netw. 10, A286–A297 (2018).
23. D. Sequeira, M. Ruiz, N. Costa, A. Napoli, J. Pedro and L. Velasco, "OCATA: a deep-learning-based digital twin for the optical time domain J. Opt. Commun. Netw. 15, 87-97 (2023).
24. A. Raj, Z. Wang, F. Slyne, T. Chen, D. Kilper and M. Ruffini, "Self-normalizing neural network, enabling one shot transfer learning for modeling EDFA wavelength dependent gain," in European Conference on Optical Communication (ECOC) (2023).
25. Y. Pointurier, "Machine learning techniques for quality of transmission estimation in optical networks," J. Opt. Commun. Netw. 13, B60-B71 (2021).
26. P. Poggiolini, G. Bosco, A. Carena, V. Curri, Y. Jiang and F. Forghieri, "The GN-Model of Fiber Non-Linear Propagation and its Applications," J. Lightwave Technol. 32, 694-721 (2014).
27. D. Semrau, R. I. Killey and P. Bayvel, "The Gaussian Noise Model in the Presence of Inter-Channel Stimulated Raman Scattering," J. Lightwave Technol. 36, 3046-3055 (2018).
28. J. Lu, G. Zhou, Q. Fan, D. Zeng, C. Guo, L. Lu, J. Li, C. Xie, C. Lu, F. N. Khan, and A. Pak Tao Lau, "Performance comparisons between machine learning and analytical models for quality of transmission estimation in wavelength-division-multiplexed systems [Invited]," J. Opt. Commun. Netw. 13, B35-B44 (2021).
29. N. Morette, I. F. de Jauregui Ruiz, and Y. Pointurier, "Leveraging ML-based QoT tool parameter feeding for accurate WDM network performance prediction," in Optical Fiber Communication Conference (OFC) (2021), paper Th4J.4.
30. R. Ayassi, A. Triki, M. Laye, E. Le Rouzic, N. Crespi, and R. Minevra "Bayesian optimization-based algorithm to improve the quality of transmission estimation," in OSA Advanced Photonics Congress (2021), paper NeF2B.3.
31. G. Borraccini, Y. Huang, A. D'Amico, T. F. de Lima, E. Ip, V. Curri, T. Wang, and K. Asahi, "Optical Line Physical Parameters Calibration in Presence of EDFA Total Power Monitors," in Optical Fiber Communication Conference (OFC) (2024), paper M3I.5.
32. N. Morette, H. Hafermann, Y. Frignac, and Y. Pointurier, "Machine learning enhancement of a digital twin for wavelength division multiplexing network performance prediction leveraging quality of transmission parameter refinement," J. Opt. Commun. Netw. 15, 333-343 (2023).
33. J. Zhou, J. Lu, and C. Yu, "Improving the accuracy of QoT estimation with insertion loss distribution evaluation for C + L band transmission systems," J. Opt. Commun. Netw. 16, 12-20 (2024).
34. Z. Cui, Y. Song, X. Luo, S. Li, J. Li, M. Fu, C. Ju, J. Li, M. Zhang, and D. Wang, "Optical fiber anomaly detection through SRS-induced spectral tilt in C+L-band transmission systems," J. Opt. Commun. Netw. 17, 616-630 (2025).
35. Y. Zhang, X. Liu, Q. Qiu, Y. Liu, L. Yi, W. Hu, and Q. Zhuge, "Mapping-finding input-parameter refinement paradigm for a dynamic multiband optical network digital twin: the Raman amplifier modeling case," J. Opt. Commun. Netw. 16, 1059-1069 (2024).
36. X. Yang, C. Sun, R. Ayassi, G. Charlet, M. Tornatore, and Y. Pointurier, "Inputs Refinement with Incremental Learning for Accurate Digital Twin of Optical Networks," in Optical Fiber Communication Conference (OFC) 2025, paper W4G.2.
37. M. Filer, J. Gaudette, Y. Yin, D. Billor, Z. Bakhtiari and J. L. Cox, "Low-margin optical networking at cloud scale [Invited]," J. Opt. Commun. Netw. 11, C94-C108 (2019).
38. S. Bigo, S. Gauchard, A. Bertaina and J. . -P. Hamaide, "Experimental investigation of stimulated Raman scattering limitation on WDM transmission over various types of fiber infrastructures," in IEEE Photonics Technology Letters, 11, 671-673 (1999).
39. A. Ferrari, M. Filer, K. Balasubramanian, Y. Yin, E. Le Rouzic, J. Kundrát, G. Grammel, G. Galimberti and V. Curri, "GNPy: an open source application for physical layer aware open optical networks," IEEE/OSA J. Opt. Commun. Netw. 12, C31-C40 (2020).
40. Y. Zhang, M. Zhang, Y. Song, Y. Shi, C. Zhang, C. Ju, B. Guo, S. Huang, and D. Wang, "Building a digital twin for large-scale and dynamic C+L-band optical networks," J. Opt. Commun. Netw. 15, 985-998 (2023).
41. C. Zhu, R. H. Byrd, P. Lu, and J. Nocedal, "Algorithm 778: L-BFGS-B, FORTRAN routines for large scale bound constrained optimization," in ACM Transactions on Mathematical Software, 23, 550-560 (1997).
42. Y. Liu, A. Zhang, K. Lv, X. Wang, L. Feng, H. Liu, X. Sheng, C. Li, S. Ji, T. Ma, T. Chang, Q. Lu, L. Han, H. Wang, D. Huang, Y. Huang, X. Liu, W. Jia, X. Huo, J. Li, C. Zhang, " Field Trial of Telecom-Grade Sub-50ms Protection in Wavelength Switched Optical Networks for Lossless Large Language Model Multi-datacenter Distributed Training," in European Conference on Optical Communication (ECOC) (2025), paper Tu.01.06.4.